
Advanced Composite Materials
Publication details, including instructions for authors and subscription information:
http://www.tandfonline.com/loi/tacm20

# Low Velocity Impact Behavior of Aluminum Honeycomb Structures

I. T. Lee [a], Y. Shi [b], A. M. Afsar [c], Y. Ochi [d], S. I. Bae [e] & J. I. Song [f]

[a] Department of Mechanical Engineering & Intelligent Systems, University of Electro-Communication Chofugaoka, 1-5-1 Chogu, Tokyo 182-8535, Japan

[b] Department of Mechanical Engineering, Changwon National University, 9 Sarim-dong, Changwon, Kyungnam 641-773, Korea

[c] Department of Mechanical Engineering, Changwon National University, 9 Sarim-dong, Changwon, Kyungnam 641-773, Korea

[d] Department of Mechanical Engineering & Intelligent Systems, University of Electro-Communication Chofugaoka, 1-5-1 Chogu, Tokyo 182-8535, Japan

[e] Department of Mechanical Engineering, Changwon National University, 9 Sarim-dong, Changwon, Kyungnam 641-773, Korea

[f] Department of Mechanical Engineering, Changwon National University, 9 Sarim-dong, Changwon, Kyungnam 641-773, Korea;, Email: jisong@changwon.ac.kr

Version of record first published: 02 Apr 2012.

VSP

*Advanced Composite Materials 19 (2010) 19–39*

ADVANCED COMPOSITE MATERIALS
brill.nl/acm

# Low Velocity Impact Behavior of Aluminum Honeycomb Structures

**I. T. Lee** [a], **Y. Shi** [b], **A. M. Afsar** [b], **Y. Ochi** [a], **S. I. Bae** [b] **and J. I. Song** [b,*]

[a] Department of Mechanical Engineering & Intelligent Systems, University of Electro-Communication Chofugaoka, 1-5-1 Chogu, Tokyo 182-8535, Japan
[b] Department of Mechanical Engineering, Changwon National University, 9 Sarim-dong, Changwon, Kyungnam 641-773, Korea

Received 1 December 2008; accepted 22 December 2008

**Abstract**
Impact behaviors of aluminum honeycomb sandwich panels (AHSPs) are investigated experimentally by using a drop weight test setup. The specimens of 12.7 mm cell size were tested by impacting at four different initial contact points, namely face center, corner, long edge and short edge of core cells, with two impactors of weights 5.25 kg and 11.9 kg, respectively. Dynamic nonlinear transient analysis was also carried out by a finite element simulation model developed based on continuum damage mechanics to account for nonlinear and elastoplastic behavior. The results revealed that while the impact behaviors of AHSPs were nearly the same for low impact energy, they were different for high impact energy. The peak resistance force of AHSPs was the highest for impact at the face center and the lowest for impact at the short edge of the core cells. The results of FE simulation revealed that the real time deformation produced fracture when the crack initiated and propagated to the honeycomb core from the facesheet.


**Keywords**
Aluminum honeycomb sandwich panel (AHSP), fracture, impact behavior, damage mechanics, finite element analysis



## 1. Introduction

Aluminum honeycomb sandwich panels (AHSPs) have been widely used in aerospace, defense, automotive, railway, marine, communication, and sport industries because of their properties of light weight, high strength and high stiffness. Also, they have excellent properties of high-energy absorption, fatigue resistance and recyclability, with the additional advantage that they are fire proof. As a particular example within the automotive industry, AHSPs have been used in components

* To whom correspondence should be addressed. E-mail: jisong@changwon.ac.kr
Edited by KSCM


DOI:10.1163/156855109X434810

of an auto body as the crush box to absorb designed impact energy efficiently during a crash accident. From the viewpoint of engineering, a honeycomb structure is well known as the ideal structural topology to meet the requirements of stable and robust designs against the sophisticated loading conditions. However, aluminum sandwich constructions using thin-gage aluminum facesheets cohered to the honeycomb cores must be investigated, as damage tolerance with their related strength changes. Some studies revealed that the pre-existed damage on the interfaces between cores and facesheets affects the strength change and impact energy [1]. It suggests that the design variables should include certain small changes, such as initial contact points or initial impact angle with inherent initial damage. AHSPs are generally used in structures under dynamic shock loading because of their eminent ability to mitigate the shock loading. Papka and Kyriakides [2] evaluated the damage mechanism after impacting by optical analysis and ultrasonic c-scan. Lim *et al.* [3] found that the test frequency is lower than the resonance frequency of honeycomb structures by using mechanical impedance method, in spite of various ways of finding the debonding in honeycomb structures [4, 5]. Kim and Christensen [6] calculated the elastic modulus, shear modulus, Poisson's ratio, compressive bending strength, shear bending strength and flexibility of the cell. They found that the triangular and star cells were weak in compressive bending and shear bending.

In a previous work [7] of two of the authors of the present paper, the variable fracture mode was found in response to the increase of the impact energy. The change of fracture mode could be measured by the impact energy loss rate. Tsai *et al.* [8] developed Green's function to analyze the upper and lower part of a honeycomb sandwich panel subjected to low velocity impact. Thwaites and Clark [9] examined the fracture behaviors of honeycomb sandwich structures using elastic wave and acoustic emission. Goldsmith and Sackman [10] checked the buckling pattern of core and analyzed small elastic energy after AHSP, aluminum core, and flex core were impacted. Santosa and Wierzbicki [11] compared the impact strengths of the honeycomb cell and foam. They found that the aluminum honeycomb could show better impact behaviors than aluminum foam under unidirectional loading and a combination of compressive and bending loads. They suggested that the crush strength of aluminum honeycomb is related to the relative density based on the directional plastic collapse stress. The force transmission of aluminum honeycomb is investigated by experimental approach under both the quasi-static and dynamic impact loading conditions followed by numerical simulation of the study [12]. Many applications of computational mechanics based on continuum damage model have been reported in various failure analysis like fatigue, ductile and brittle, creep and creep–fatigue, and dynamic failures [13–17].

In this study, a typical impact fracture mode was investigated. Experimental time history data such as force and the impact damage area observed with ultrasonic c-scan were directly compared with finite element simulation results. To take into account the failure mechanism, the real time deformation process was analyzed and related to physical variables with synchronized post-processing. For finite element

simulation, Hyper Works 9.0 was used for pre- and post-processing while LSdyna V971 was used for calculation.

## 2. Experimental and Finite Element Analysis

### 2.1. Dynamic Impact Experiment

An eperiment was conducted with a drop weight test setup as shown in Fig. 1. A dynatup GRC8250 drop tower (Instron) was used in which an embedded measuring device recorded the dynamic loading history triggered by a velocity sensor of laser beam type while the stainless rigid tup (SS400) started to hit and penetrated into the AHSP.

The AHSP specimens received from Hankuk Fiber Ltd were fabricated by adhesive bond between A3003H14 facesheets and hexagonal cell cores. The material properties of the specimens and the tup are listed in Table 1.

The AHSPs with core cells of width 12.7 mm were tested and two impactors of respective weights 5.25 kg and 11.9 kg were used to vary the impact energy. The

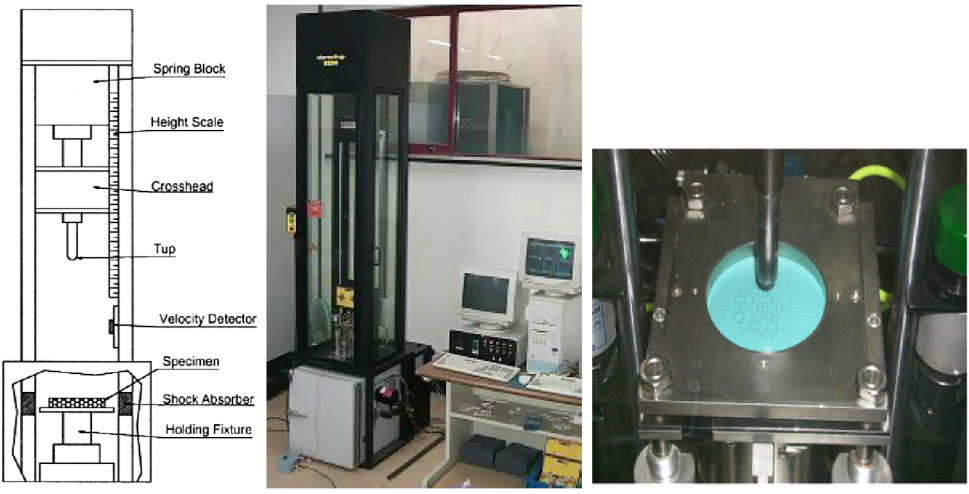


**Figure 1.** Dynamic drop weight test setup and AHSP specimen. This figure is published in color on http://www.ingentaconnect.com/content/vsp/acm

**Table 1.**
Mechanical properties of specimen and tup

| Material | Tensile strength $\sigma_u$ (MPa) | Yield strength $\sigma_y$ (MPa) | Elongation $\varepsilon$ (%) | Young's modulus $E$ (GPa) | Mass density $\rho$ (g/cm$^3$) |
|---|---|---|---|---|---|
| A3003H14 | 208 | 125 | 45 | 69 | 2.73 |
| SS400 | 400 | 235 | 20 | 210 | 7.85 |

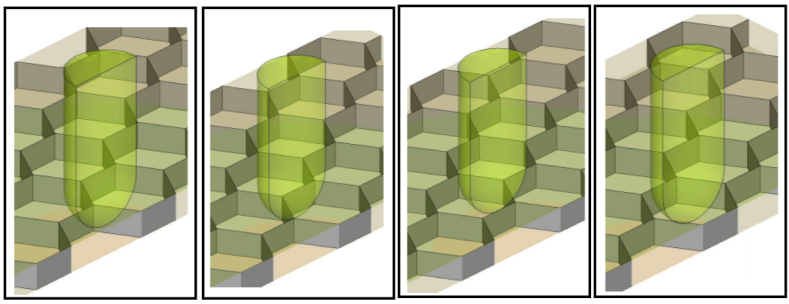


**Figure 2.** Initial contact point between tup and AHSP core cell. This figure is published in color on http://www.ingentaconnect.com/content/vsp/acm



AHSP specimens were acquired in the form of real production line with a size of 100 mm × 100 mm × 6 mm fabricated from 1 mm and 0.5 mm facesheets. The core height and core wall thickness were 4.5 mm and 0.0762 mm, respectively. For the purpose of clamping, specimens were provided with 75 mm diameter circular clamping devices attached on the AHSP top and bottom surfaces. A hemispherical rigid tup with 12.7 mm diameter was dropped on the AHSP and the initial contact points were varied around the hexagonal honeycomb cell edge to study the mechanism of AHSP failure process. Four initial contact points were considered around the hexagonal honeycomb cell edge. These four initial contact points are face center, corner, long edge and short edge as shown in Fig. 2.

The impact velocity was varied by varying the tup weight and height and the amount of energy was calculated by considering the equation of gravitational potential energy. This potential energy can be thought of that energy stored due to deformation and released due to cracking to failure. The combination of mass and height of the tup gave different gravitational energy for each test. Eight different initial impact velocities were derived from gravitational potential energy by using two different weights of tup and four different heights for each of these tups as shown in Table 2. The corresponding impact energy as shown in Table 2 was intentionally increased by an amount of about 10 J in each step.

### *2.2. Finite Element Analysis*

To simulate the actual fracture process accompanying large deformation, the updated Lagrangian was used to account for large strains and displacements. Symmetric conditions were not applied, because contact points were varied in this study and the elastic stress wave and deflection might not be exactly symmetric even if symmetric clamped boundary was used (Fig. 3). Furthermore, the interaction between the clamp plate and the facesheet of AHSP is also important to decide the crack initiation by critical deflection of the facesheet. The first strategy is to use meshes patterning a radially directed grid line but it is not orthogonal to the core

**Table 2.**
Kinetic energy from different mass and initial height

| Impact weight | Impact height (cm) | Impact velocity (m/s) | Impact energy (J) |
|---|---|---|---|
| 11.9 kg | 8.6 | 1.3 | 10 |
| | 16.3 | 1.78 | 19 |
| | 27.4 | 2.32 | 32 |
| | 36.9 | 2.69 | 43 |
| 5.25 kg | 19.5 | 1.95 | 10 |
| | 37 | 2.69 | 19 |
| | 62 | 3.49 | 32 |
| | 83.5 | 4.05 | 43 |

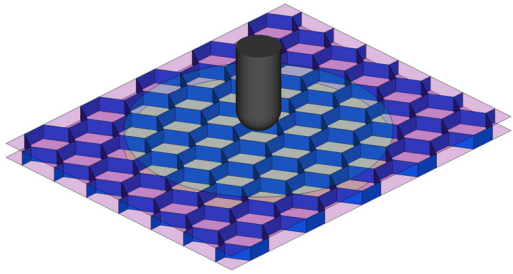

**Figure 3.** Finite element model for dynamic drop test (full model). This figure is published in color on http://www.ingentaconnect.com/content/vsp/acm

shells, because it prevents zipping in straight line tear mode that affects the failure strength and toughness. To model actual material behavior, anisotropic elasto-visco-plasticity is used in combination with an isotropic hardening model. Damage is also coupled with this material law. To obtain material parameters, tension test on A3003 H14 at room temperature is performed and the observed behavior is shown in Fig. 4.

## 3. Results and Discussion

### *3.1. Test Results*

#### *3.1.1. Drop Impact Test*

Figure 5 shows the failure patterns of AHSPs corresponding to low kinetic energy of tup and consequently no penetration of the tup is found to occur. To characterize different failure patterns, the specimens were impacted at four different initial contact points, namely, face, corner, long edge, and short edge, and the resulting failure patterns are shown in Fig. 5(a–d), respectively.

Shown in Fig. 6 are the profiles of failure with tup penetration after impact at four different initial contact points. Each failure pattern looks different, which illustrates the structural built-in loading path for associated failure condition. Simply,

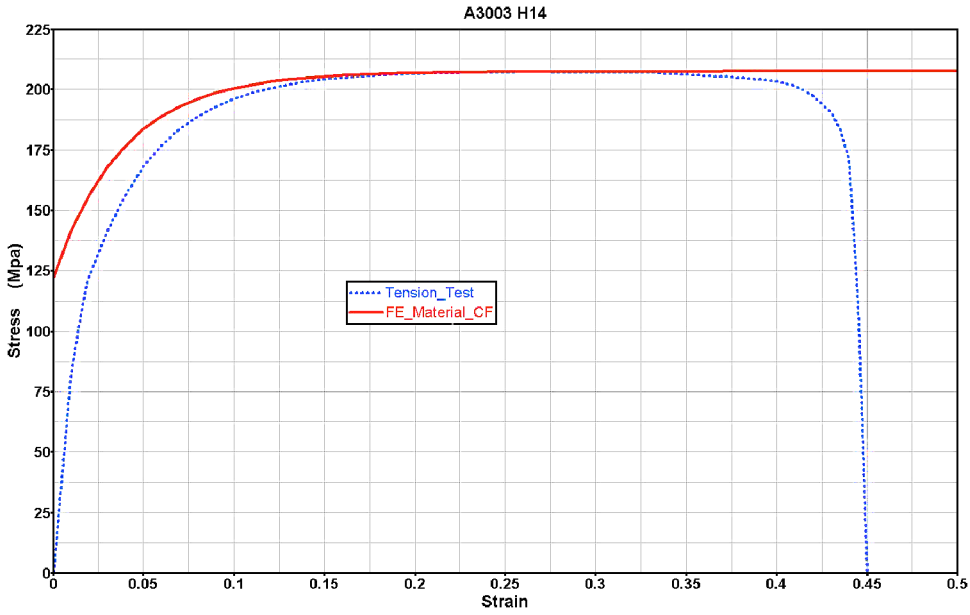


**Figure 4.** Monotonic stress–strain curves for A3003H14. This figure is published in color on http://www.ingentaconnect.com/content/vsp/acm


**Figure 5.** The profile of failure without tup penetration after impact test (5.25 kg): (a) face/34 J, (b) long-edge/19 J, (c) short-edge/19 J, (d) corner/19 J. This figure is published in color on http://www.ingentaconnect.com/content/vsp/acm

the walls of core cells are the media to transfer the load between the facesheets and lead the local crack initiation on the facesheets. Exceptionally, the case of face contact shows the wall surrounded and centered crack initiation as the wall of core cell is not directly related in crack initiation. The tup penetrates into the core with im-

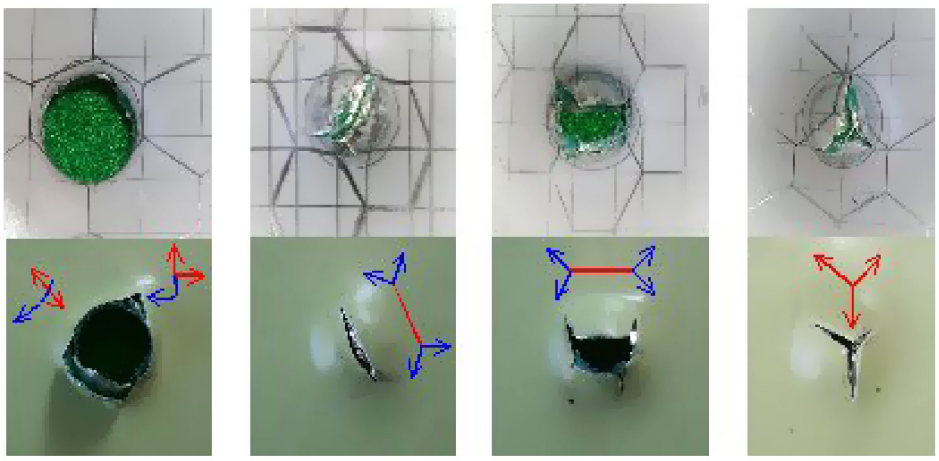


**Figure 6.** The profile of failure with tup penetration after impact test (11.9 kg). This figure is published in color on http://www.ingentaconnect.com/content/vsp/acm

pact energy of 43 J and other impact energies do not show the penetration of the tup. For 32 J impact energy, the impact on the face of the cores does not show a critically damaged area while the other cases, i.e., the impacts on the corner, short edge and long edge, show cracking over critically damaged area before perforation. This illustrates that the critical damage (meso-crack) is initially developed by core shell wall resulting in cutting the sheet panel when accumulated strain reaches the critical damage threshold. Deformation and spreading of its area developed by the edges of the core shell implicitly determine the strength of AHSPs.

To investigate the failure strength related failure mode, the impact forces were measured for each of the impact velocities and tup weights. As shown in Figs 7 and 8, the impact load time history displays a similar tendency to the impact load–deflection curve. When an 11.9 kg impact is applied to AHSPs of 12.7 mm cell width, the impulsive load appears to increase with the increase of impact energy, as shown Fig. 7. In Fig. 7(a and b) corresponding to 10 J and 19 J impact energy, respectively, the rounded peak curves represent the characteristics without a critically damaged area. But in the case of Fig. 7(c) corresponding to the impact energy of 32 J, the curves show the different peak forces and patterns (rounded and sharp) for different initial contact points. Detailed investigation of the damaged area and cracks on the surface of the facesheets indicates that the partially cracked facesheet shows sharp peak patterns and no crack facesheet shows rounded peak patterns. Consequently, the impact energy of 10 J and 19 J cannot produce great damage to AHSPs. But for 32 J impact energy, partial cracking appears in the case of edge contact impact, while the face contact impact produces no cracking anywhere.

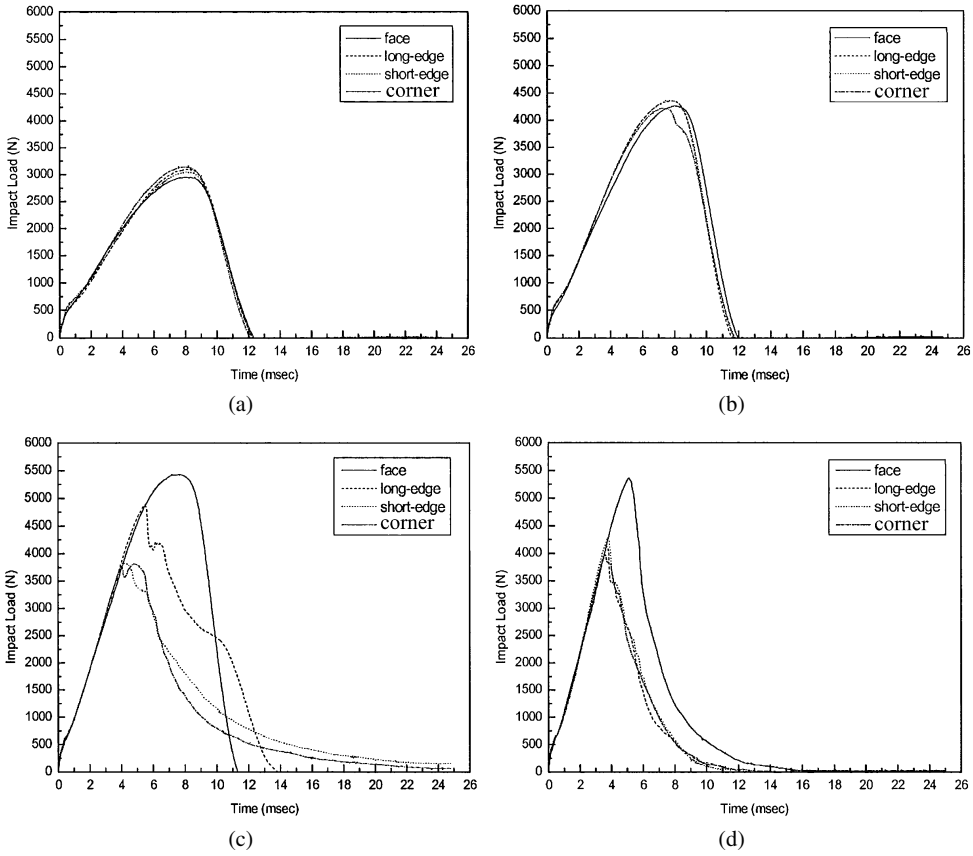


**Figure 7.** Impact load of 12.7 mm AHSP cell corresponding to 11.9 kg impactor. (a) 10 J, (b) 19 J, (c) 32 J and (d) 43 J.

The impact energy of 43 J produces considerable damage in all the cases of face, corner, short-edge, and long-edge contact impacts and shows penetration of the tup. This explains the mechanism of fracture process as the core shell edge, delivering enough shear force to the lower part of the adjacent core facesheet, leading to the development of high local strain and initiation of meso-crack at the threshold of critical damage. Particularly, the core shell imparts rigid path after compacted collapse causes early fracture for edge contact impact but face contact impact has no direct path from collapsed core shell edge so that fracture cannot occur on the facesheet.

The impact force time history of 5.25 kg impactor series is shown in Fig. 8. The cell size is the same as previous case, i.e., 12.7 mm. The curves corresponding to 5.25 kg and 11.9 kg impactors appear to have a similar tendency. However, because of the unequal weight and different impact height, the initial slopes and peaks of the curves are slightly different and high for high initial velocity for lower weight. This explains the loading rate dependency of mechanical properties such as strength and

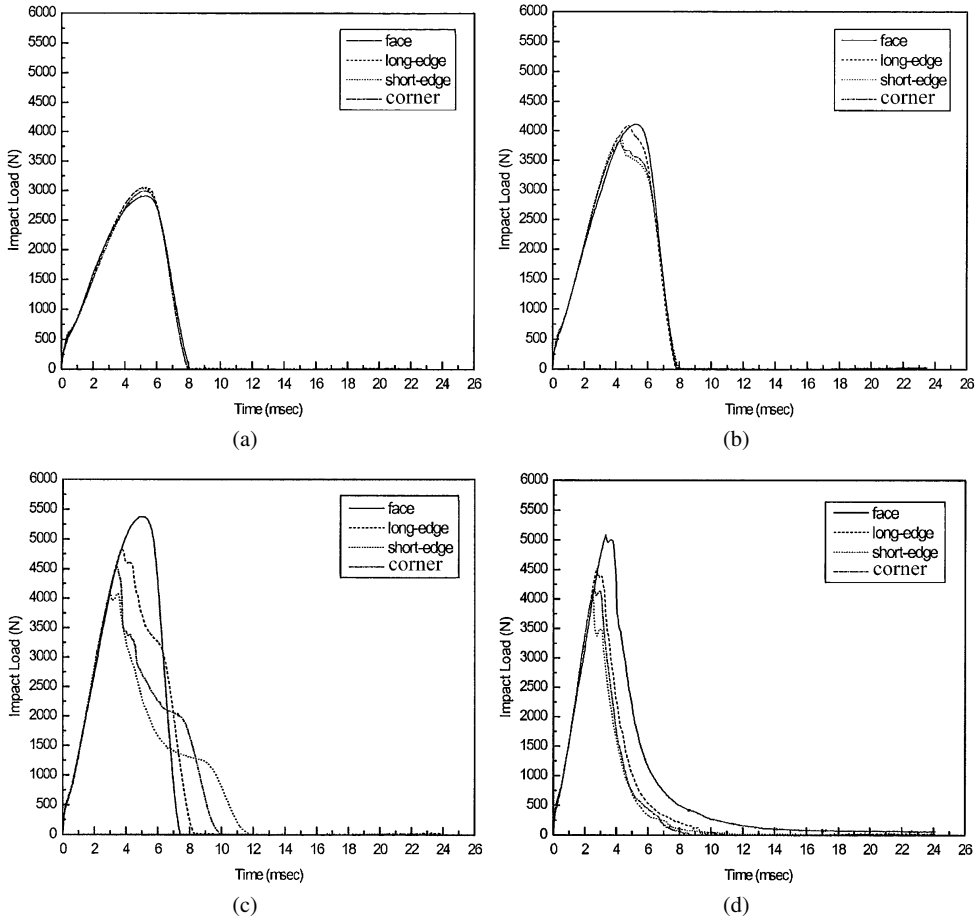


**Figure 8.** Impact load of 12.7 mm AHSP cell corresponding to 5.25 kg impactor. (a) 10 J, (b) 19 J, (c) 32 J and (d) 43 J.

absorbed energy. To understand this fact, the time required to achieve the peak force was investigated and shown in Table 3.

The lower mass generates the higher speed to have equal impact energy and less deformation until the peak force is attained which, in turn, produces less damaged area. Peak force is not sensitive to the change of loading late. This means that the strength is a function of deformation and deformation rate along with corresponding constitutive material properties at the loading speed range of up to critical damage threshold.

The relative peak force and the corresponding time to attain this value of peak force are identified easily along with loading rate as shown in Fig. 9. The peak force is increased with loading rate (potential energy). After over critical damage, the peak force is not changed so much, because of crack propagation and released energy. Further, the stored energy until the peak force decreases with the increase

**Table 3.**
Impact duration with raising time and fading out (impact point: face)

| Impact weight | Impact velocity (m/s) | Rising time to peak (ms) | Peak force (kN) |
|---|---|---|---|
| 11.9 kg | 1.3 | 8.5 | 2.9 |
| | 1.78 | 8 | 4.2 |
| | 2.32 | 4 (f) to 8 | 4.8 (f) to 5.4 |
| | 2.69 | 4 (f) to 6 | 4.2 (f) to 5.4 |
| 5.25 kg | 1.95 | 5.5 | 2.9 |
| | 2.69 | 5 | 4.2 |
| | 3.49 | 4 (f) to 6 | 4.7 (f) to 5.3 |
| | 4.05 | 3 to 5 | 4.4 (f) to 5.1 |

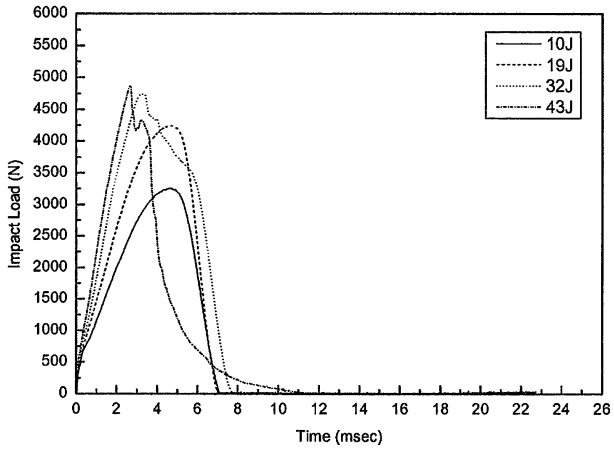


**Figure 9.** Effect of loading rate on impact force corresponding to 5.25 kg impactor (face).

of loading rate. However, the stored energy increases with increasing the loading rate when there is no cracking.

*3.1.2. Absorbed Energy*

The state potential of the material is described with the stored energy and dissipated energy. Accompanying the deformation, failure and elastic recovery are coupled with each other. Energy is often used for quantitative indication of how much strain with associated stress work is accumulated for a material state, and its scalar quantity gives the indication of change of state. Figure 10 shows the energy curve which is composed of dissipated damage energy and plastic and elastic stored energy. Based on these energy curves, each of the energy components is summarized in Table 4. The maximum absorbed energy is taken as the maximum value from energy time history. Finally, the elastic or dissipated energy is simply calculated by subtracting plastic energy from the maximum energy.

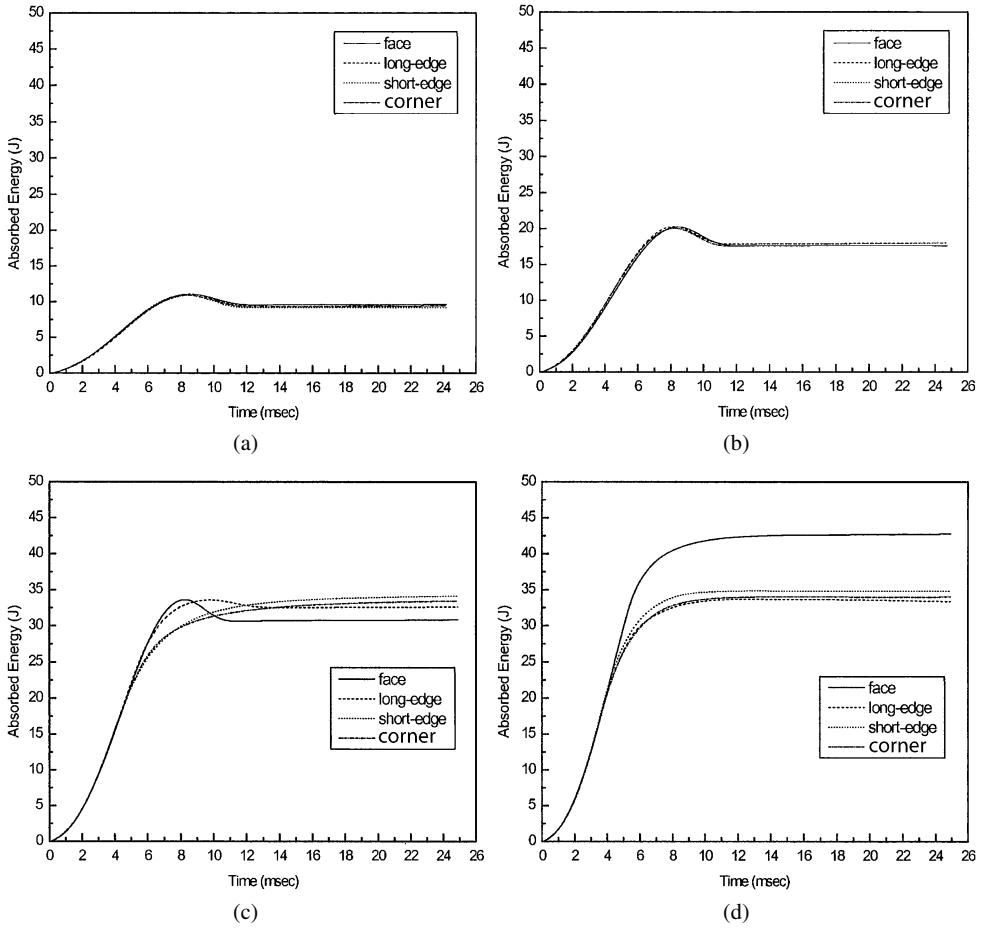


**Figure 10.** Absorbed energy of 12.7 mm AHSP cell (11.9 kg). (a) 10 J, (b) 19 J, (c) 32 J and (d) 43 J.

**Table 4.**
Energy contribution (unit: J, impact point: face)

| Weight | Velocity (m/s) | Max energy | Plastic | Elastic or dissipated |
|---|---|---|---|---|
| 11.9 kg | 1.3 | 11 | 9 | 2 |
| | 1.78 | 20.5 | 17.8 | 2.7 |
| | 2.32 | 34 (33) | 31 (22) | 3 (F11) |
| | 2.69 | 43 (34) | 30 (23) | F13 (F11) |
| 5.25 kg | 1.95 | 10.5 | 9 | 1.5 |
| | 2.69 | 20 | 17.8 | 2.2 |
| | 3.49 | 32.5 (32) | 29 (23) | 3.5 (F9) |
| | 4.05 | 43 (35) | 27 (23) | F16 (F12) |

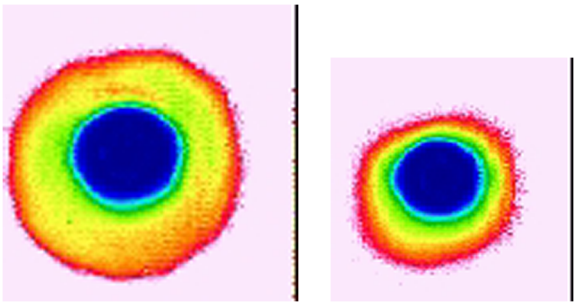

(a) (b)

**Figure 11.** Ultrasonic c-scan image (face/32 J): (a) 11.9 kg and (b) 5.25 kg. This figure is published in color on http://www.ingentaconnect.com/content/vsp/acm



It is not possible to explain exactly the crack propagation mechanism with these energies; however, it is presumed that the critical damage starts at the global peak force of around 23 J impact energy, whatever crack propagates and spreads out with each loading case. The different loading conditions produce a different evolution to the total failure, which is mainly depended on the facesheet's damaged area as the face contact case requires more energy for global failure than any other cases.

Performing an ultrasonic c-scan is known as a useful method to observe damage after impact. To investigate the damage evolution size before the global failure, two cases of different masses for the face contact impact are selected. Figure 11 shows the c-scan images of the damage surface. From this figure, we can find that the afloat area of 11.9 kg impact force with 32 J impact energy in the 12.7 mm cell size specimen is larger than that of 5.25 kg. This means that the heavier tup with about the same impact energy creates the bigger damage face, which explains that damage evolution is a function of speed and damage parameters have to be fully coupled with strain rate of elasto-plasticity.

### *3.2. Results of FE Analysis*

The ruptured, partially damaged, and plastically deformed shapes are compared in Fig. 12. Like test results, perfect penetration of tup occurs only at 43 J impact energy and others show partially damaged and pure plastic deformation.

For all the face, corner and edge contact impacts, perforation occurs when impact energy is 43 J. On the other hand, partial breakage is found to occur at 32 J impact energy in the case of corner and edge contact impact only. The simulation results also show large plastic deformation without any breakage in all the cases of face, corner, and edge contact impacts when the impact energy is below 19 J. Like the results shown in Figs 5 and 6, FE simulation also shows successful representation of failure mode in honeycomb structures. The crack line along the edge of core cells is observed to be the same as experimental results.

To make an analysis of dynamic fracture mechanism, the detailed snapshots are taken from FE simulation results as shown in Figs 13 and 14. Taking advantage of

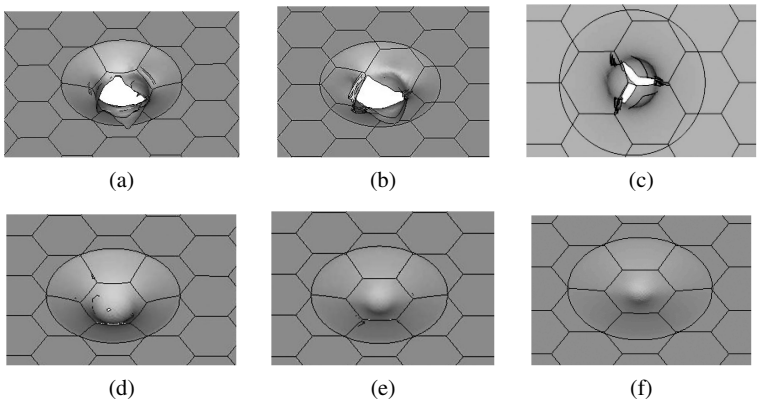


**Figure 12.** Perforation, partial cracking and deformation mode: (a) face/11.9 kg/43 J, (b) corner/11.9 kg/43 J, (c) corner/11.9 kg/32 J, (d) face/5.25 kg/32 J, (e) face/5.25 kg/19 J and (f) face/5.25 kg/10 J.

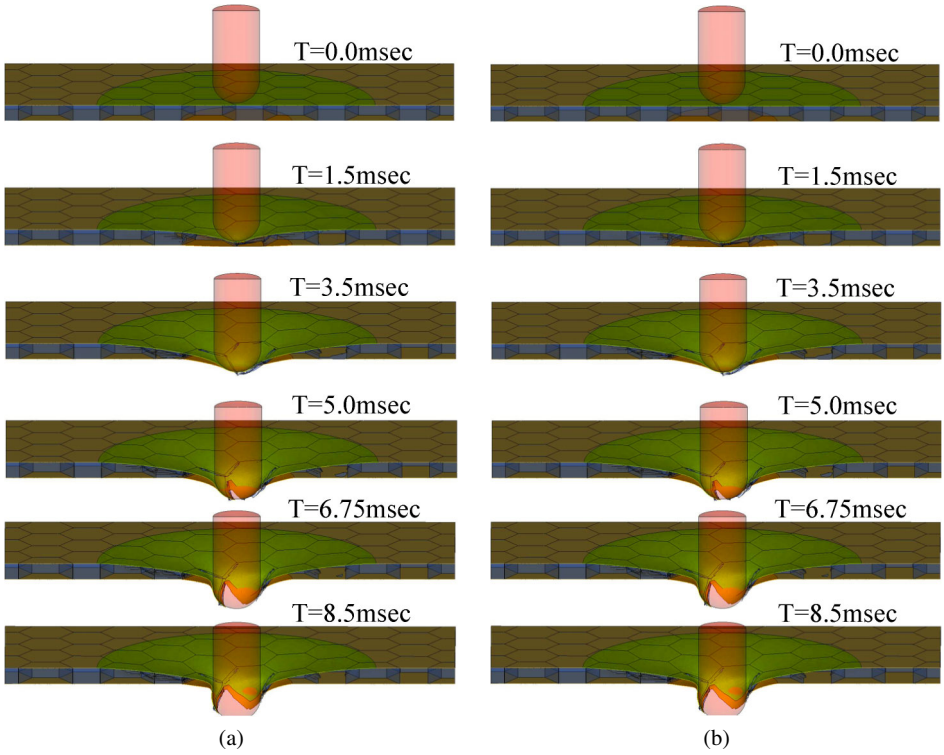


**Figure 13.** Tearing of the facesheet and perforation process (11.9 kg/43 J). (a) Corner contact and (b) face contact. This figure is published in color on http://www.ingentaconnect.com/content/vsp/acm

the FE simulation, sectional views are presented for exact analysis of the detailed deformation process and start of tearing with its time history curve.

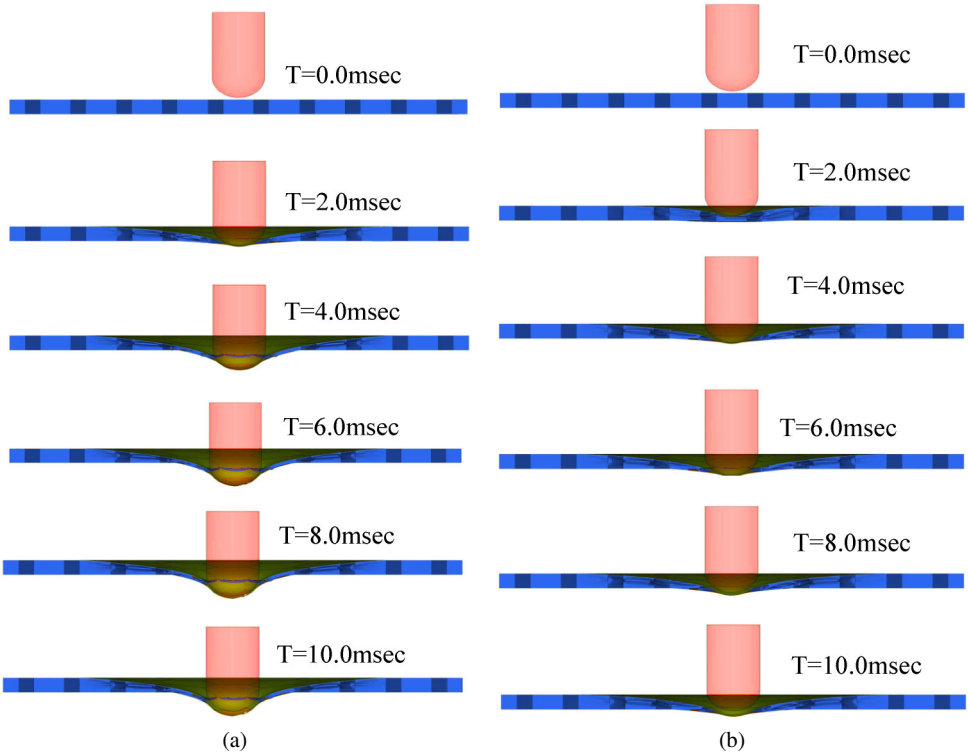


**Figure 14.** Non-perforation at lower kinetic energy of 5.25 kg tup (32 J). (a) Corner contact and (b) face contact. This figure is published in color on http://www.ingentaconnect.com/content/vsp/acm

In order to validate the FE simulation results, two perforation and five non-perforation cases are compared by means of time history and deformation pictures taken from FE simulation. Unlike the limitations of the practical test, FE simulation gives tremendous post-processing facilities to analyze deformation and failure process with time history and related deformed shape.

For the case of corner impact, the edges of core cells directly transfer the impact load by touching the tup surface and core cells retain rigidity after buckled compaction so that the cracking time of the facesheet occurs before the face contact impact. This is identified by the fact that the force is dropping after around 3 ms for corner impact and 3.5 ms for the face impact, as shown in Fig. 15.

In contrast with the edge impact to cause cracking, the face impact shows the crack initiation after sticking of the upper and lower facesheets together and the crack is initiated first on the upper facesheet, which is more stretched around the core cell than the lower.

Cracking of the upper sheet causes the lower to be strained to cracking, so it takes time to reduce the load before showing the rebound compliance with formation of a small plateau. The experimental force time history shown in Figs 7 and 8 also displays this plateau and two peaks at the lower loading rate apparently.

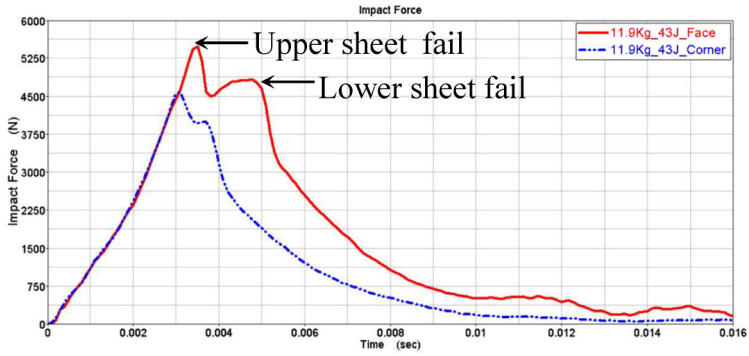


**Figure 15.** Impact force time history from FE simulation (sampling rate: 10 kHz). This figure is published in color on http://www.ingentaconnect.com/content/vsp/acm

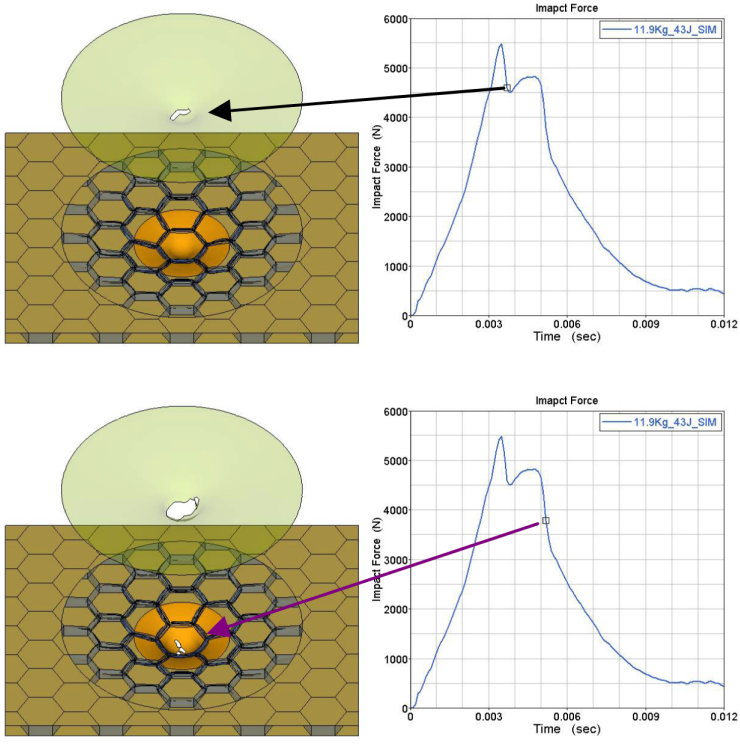


**Figure 16.** Crack development during impact loading (face). This figure is published in color on http://www.ingentaconnect.com/content/vsp/acm

Since accurate cracking time determination is important to understand the force time history, several snapshots are synchronized with the time history curve and presented in Fig. 16. To easily find out what happens during the perforation, the upper facesheet is displayed with an exploded view and time is synchronized at

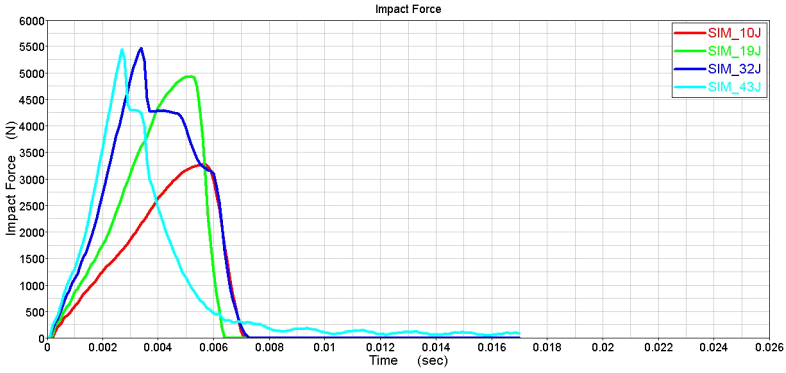


**Figure 17.** Force time history along with loading rate (11.9 kg/face). This figure is published in color on http://www.ingentaconnect.com/content/vsp/acm

the deformation progression. The onset of cracking was not detected in this picture, but the size of crack is presumably developed soon after the peak force on the upper sheet, and the cracking on the lower sheet is started after the second peak force while the previous cracking on the upper sheet is being widened. This described time lag between upper and lower facesheet cracking is a characteristic of this AHSP for which the optimum structural loading curve is explicitly derived by the core height, size, and initial contact point, which directly influences the load time history.

As shown in Fig. 17, the increase of loading rate increases the peak force, which is very similar to the test results shown in Fig. 9 and thus establishes the consistency between the test and the FE simulation. The FE peak force is around 10% higher than that of the test and the time of peak force is slightly longer than that of the test.

One additional discussion point and validation, which is seldom reviewed in the fabrication problems, is the contribution rate for energy absorption. For this purpose, the total absorbed energy that is measured by experiment (Fig. 10) is set for validation and then the energy absorbed by each material component is discussed. Figure 18 shows the energy balance, which is the kinetic energy of the tup and the summation of the internal energy of each component arising from deformation.

The material internal energy of all the components is summed as 36 J, which is 84% of the kinetic energy (43 J) of the tup. The ratio of these energies (84%) is the indication of how much kinetic energy is transformed into deformation energy. The remaining 16% energy is the summation of the strain energy released (dissipation) due to cracking and kinetic energy still possessed by the tup after penetration. In contrast with the fractured case, the lower kinetic energy of the tup without any failure of the AHSP shows perfect transformation from kinetic energy to internal deformation energy including elastic deformation energy.

Figure 19 shows the energy time history corresponding to 19 J impact energy, which is seen to be similar to that of 43 J impact energy. Unlike the case of 43 J impact energy, however, here elastic rebound is observed as in the test results. The

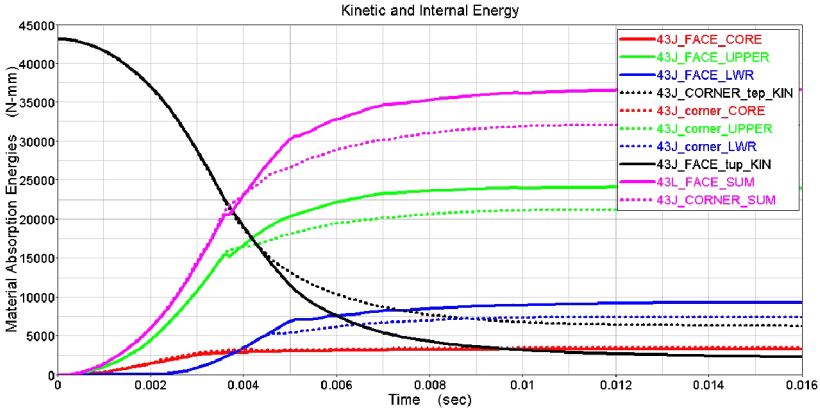


**Figure 18.** Material internal and kinetic energy curves (11.9 kg/43 J). This figure is published in color on http://www.ingentaconnect.com/content/vsp/acm

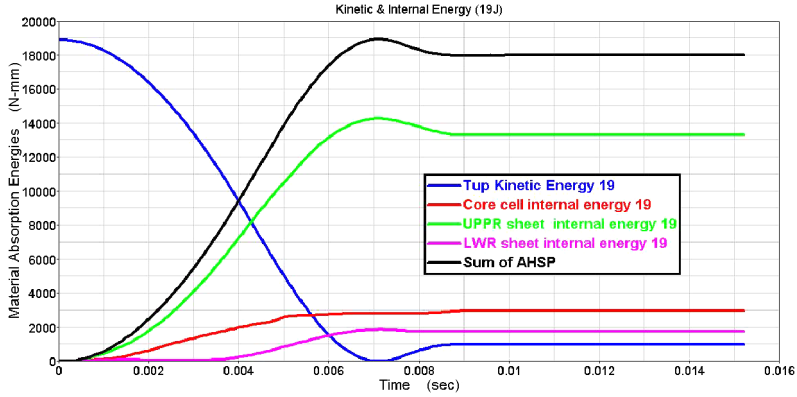


**Figure 19.** Material internal and kinetic energy curve (11.9 kg/19 J/face). This figure is published in color on http://www.ingentaconnect.com/content/vsp/acm

measured total internal energy including the elastic store energy of 1 J is found to be same as 19 J.

The internal energies of the upper facesheet are 71.1% and 55.8% corresponding to the 19 J and 43 J impact energy, respectively. The energy contribution for the case of 11.9 kg tup is summarized in Table 5. The energy of dissipation is the associated strain energy for damage evolution up to the critical damage of meso-crack initiation. This energy is separately represented as deformation energy but strongly coupled with elasto-visco-plastic law. This means that this dissipation energy can be regarded as work energy for micro crack propagation. A dissipation energy of 4.5 J is required to penetrate the thickness of the AHSP in the case of 43 J impact.

The brace in the case of the corner impact shows less deformation, implying more kinetic energy still possessed by the tup, which in turn consequently means easy perforation of the AHSP depth. For the case of the impact with 5.25 kg tup, the energy contribution is summarized in Table 6. Almost the same amount of energy

**Table 5.**
Internal energy contribution (11.9 kg/face)

| Components | | Internal energy (J) | Ratio (%) |
|---|---|---|---|
| 43 J | Core | 2.8 (3.4) | 6.5 (7.9) |
| | LOWER | 9.2 (7.5) | 21.4 (17.4) |
| | UPPER | 24 (21) | 55.8 (48.8) |
| | Elastic | – | – |
| | Dissipation | 4.5 (4.8) | 10.4 (11.2) |
| | Kinetic | 2.5 (6.3) | 5.8 (14.7) |
| 19 J | Core | 2.8 | 14.7 |
| | LOWER | 1.7 | 8.9 |
| | UPPER | 13.5 | 71.1 |
| | Elastic | 1 | 5.3 |
| | Dissipation | – | – |
| | Kinetic | – | – |

**Table 6.**
Internal energy contribution (5.25 kg/face)

| Components | | Internal energy (J) | Ratio (%) |
|---|---|---|---|
| 43 J | Core | 2.8 | 6.5 |
| | LOWER | 9.4 | 21.4 |
| | UPPER | 24.2 | 55.8 |
| | Elastic | – | – |
| | Dissipation | 4.1 | 10.4 |
| | Kinetic | 2.5 | 5.8 |
| 32 J | Core | 2.8 | 8.75 |
| | LOWER | 7.2 | 22.5 |
| | UPPER | 20.5 | 64.1 |
| | Elastic | 0.4 | 1.3 |
| | Dissipation | 1.1 | 3.4 |
| | Kinetic | – | – |
| 19 J | Core | 2.5 | 13.2 |
| | LOWER | 2.2 | 11.6 |
| | UPPER | 12.9 | 67.9 |
| | Elastic | 1 | 5.3 |
| | Dissipation | – | – |
| | Kinetic | – | – |
| 10 J | Core | 1.8 | 18 |
| | LWR | 0.5 | 5 |
| | UPPER | 7.2 | 72 |
| | Elastic | 0.5 | 5 |
| | Dissipation | – | – |
| | Kinetic | – | – |

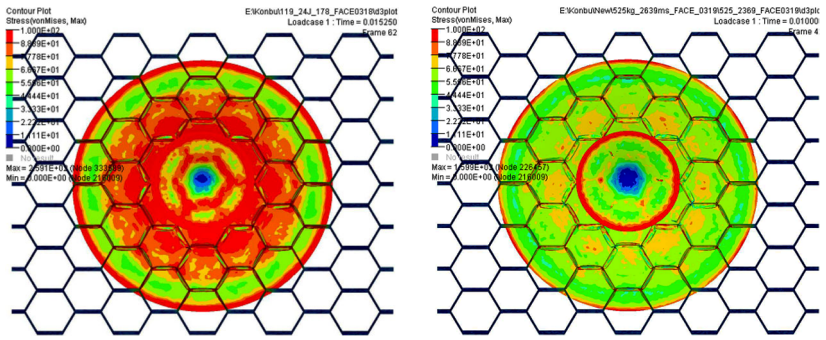


(a) (b)

**Figure 20.** Stress distribution after complete rebounding (face): (a) 11.9 kg/19 J and (b) 5.25 kg/19 J. This figure is published in color on http://www.ingentaconnect.com/content/vsp/acm

is required to penetrate the thickness of the AHSP indicating that the loading rate is not sensitive to deformation and dissipation energy. The internal energy attained by the core cell is 1.8–2.8 J. Thus, the core cell itself is not the major component for energy absorption, but it could change the loading path to cause more deformation of the AHSP.

In order to compare small damage area without meso-crack, von Mises stress distributions of FE simulation after complete bounce are plotted in Fig. 20. Similar to the ultrasonic c-scan image, the impact with the heavier tup shows a large stressed area. This means that the high loading rate causes less spreading of stress and deformation in every direction of the AHSP and the damage model describes well the damage rate as a function of strain rate.

## 4. Conclusions

Dynamic drop tests were conducted to characterize the deformation and fracture mechanism of an AHSP in response to the low velocity impact. To achieve this goal, drop tests were performed at various loading rate and different local initial contact points of the core cells.

To simulate the fracture mechanism and deformation of the AHSP, a FE modeling was also developed and simulation results of various parameters such as stress, strain, component energy, force history, sectional deformation, and fracture patterns were compared with those of experiment. In the FE simulation, the damage model was fully coupled with elasto-visco-plasticity. The comparison of the results led to the following conclusions:

1. Loading rate is not sensitive to the maximum dynamic load. However, at the initial loading stage before reaching the maximum load, the slope of loading linearly increases with the increase of loading rate.

2. For low impact energy, the impact behaviors are similar for impacts at different local initial contact points on the cell cores of AHSPs. However, for high impact

energy, the behaviors are different for impacts at different contact points such as face, corner, and short and long edges of the core cells. The AHSP is found to be strongest to sustain the face impact with a large and distributed deformation. The core cell is also an important factor to change the loading path in order to prevent local tear of the upper and lower facesheets.

3. Under the same impact energy, the heavier impact tup needs more time to reach the maximum impact load than the lighter impact tup, which is attributed to the loading speed. The strain spreads out slowly and then slowly rebounds or the crack propagates with a heavier tup. A wider damage area is engendered, which is confirmed by ultrasonic c-scan image and stress distribution of FE simulation. The measured time history of energy and force agree well with the FE modeling fully coupled with the elasto-visco-plasticity.
4. The finite element simulation reveals that if the speed is faster, the time to reach the maximum stress is shortened to increase the speed. Impact damage increases locally, which indicates that the speed is the main variable to generate localized damage. This is analogous to the damage evolution as a function of strain rate.
5. The energy required to perforate the AHSP is 36–36.4 J for plastic deformation and 4.1–4.5 J for dissipation as known quantitatively by FE simulation.

*Acknowledgement*

This work and one author were partially supported by the Second Stage of Brain Korea21 Project Corps.

## References

1. D. M. McGowan and D. R. Ambur, Damage characteristic and residual strength of composite sandwich panels impacted with and without a compression loading, in: *Mater. Conf. Exhibit AI AA/ASME/AHS Adaptive Structures Forum, Baltimore, USA — Part 1*, pp. 713–723 (1998).
2. S. D. Papka and S. Kyriakides, Experiments and full-scale numerical simulations of in-plane crushing of a honeycomb, *Acta Materialia* **46**, 2765–2776 (1997).
3. M. K. Lim, S. C. Low, L. Jiang and K. M. Liew, Dynamic characteristics of disbonds in honeycomb structures, *Engng Struct.* **17**, 7–38 (1995).
4. A. N. Palazotto, Low velocity impact damage characteristics of Z-fiber reinforced sandwich panels-an experimental study, in: *Proc. 38th AIAA/ASME/ASCE/AHS/ASC Structures, Orlando, Florida, USA — Part 3*, pp. 3–9 (1997).
5. T. Y. Reddy, H. M. Wen, S. R. Reid and P. D. Soden, Penetration and perforation of composite sandwich panels by hemispherical and conical projectiles, *J. Pressure Vessel Technol.* **120**, 186–194 (1998).
6. B. K. Kim and R. M. Christensen, Basic two-dimensional core types for sandwich structures, *Intl J. Mech. Sci.* **42**, 657–679 (2000).
7. B. I. Kim, B. W. Noh, Y. W. Choi, S. I. Bae and J. I. Song, Dynamic fracture analysis of aluminum honeycomb sandwich panel, *Key Engng Mater.* **306**, 67–72 (2006).

8. C. Z. Tsai, E. B. Wu and B. H. Luo, Forward and inverse analysis for impact on sandwich panels, *AIAA J.* **36**, 2130–2136 (1998).
9. S. Thwaites and N. H. Clark, Non-destructive testing of honeycomb sandwich structures using elastic wave, *J. Sound Vibr.* **187**, 253–269 (1995).
10. W. Goldsmith and L. S. Sackman, An experimental study of energy absorption in impact on sandwich plates, *Intl J. Impact Engng* **12**, 241–262 (1992).
11. S. Santosa and T. Wierzbicki, Crash behavior of box columns filled with aluminum honeycomb or foam, *Computers and Structures* **68**, 343–367 (1998).
12. E. B. Wu, C. Z. Tsai and B. H. Luo, Low-velocity impact of laminated honeycomb sandwich panels, in: *Proc. First Asian-Australasian Conf. Compos. Mater. — ACCM-1, Osaka, Japan*, pp. 745–748 (1998).
13. H. P. William, R. M. Gorman and H. H. Donald, Acoustic emission signals in thin plates produced by impact damage, *J. Acoust. Emission* **17**, 29–36 (1999).
14. W. Goldsmith and J. L. Sackman, Energy absorption by sandwich plates: a topic in crashworthiness, in: *Proc. Symp. Crashworthiness and Occupant Protection in Transportation System*, Wichita State University, USA, pp. 1–30 (1991).
15. J. Lemaitre and R. Desmorat (Eds), *Engineering Damage Mechanics*. Springer Verlag, Berlin (2005).
16. D. R. J. Owen and E. Hinton (Eds), *Finite Elements in Plasticity: Theory and Practice*. Pineridge Press, Swansea, UK (1980).
17. S. Oller, O. Salomon and E. Onate, A continuum mechanics model for mechanical fatigue analysis, *Computat. Mater. Sci.* **32**, 175–195 (2005).